

A Novel Interpretation of the Radon Transform's Ray- and Pixel-Driven Discretizations under Balanced Resolutions

Richard Huber¹[0000-0003-1743-6786]

Technical University of Denmark
 Department of Applied Mathematics and Computer Science
 2800 Kgs. Lyngby, Denmark
 richu@dtu.dk

Abstract. Tomographic investigations are a central tool in medical applications, allowing doctors to image the interior of patients. The corresponding measurement process is commonly modeled by the Radon transform. In practice, the solution of the tomographic problem requires discretization of the Radon transform and its adjoint (called the back-projection). There are various discretization schemes; often structured around three discretization parameters: spatial-, detector-, and angular resolutions. The most widespread approach uses the ray-driven Radon transform and the pixel-driven backprojection in a balanced resolution setting, i.e., the spatial resolution roughly equals the detector resolution. The use of these particular discretization approaches is based on anecdotal reports of their approximation performance, but there is little rigorous analysis of these methods' approximation errors. This paper presents a novel interpretation of ray-driven and pixel-driven methods as convolutional discretizations, illustrating that from an abstract perspective these methods are similar. Moreover, we announce statements concerning the convergence of the ray-driven Radon transform and the pixel-driven backprojection under balanced resolutions. Our considerations are supported by numerical experiments highlighting aspects of the discussed methods.

Keywords: Radon Transform · Computed Tomography · Discretization Errors · Numerical Analysis · X-Ray Transform.

1 Introduction

Computed Tomography (CT) is a crucial tool in medicine, allowing the investigation of the interior of patients' bodies [10]. The measurement process consists of emitting radiation that travels through the patient, the intensity of which is then measured by a detector on the other side. This paper considers planar geometries (i.e., ignoring the third spatial dimension) with the patient's body located inside the two-dimensional unit ball $\Omega := B(0, 1) \subset \mathbb{R}^2$ (called the spatial domain). The radiation is assumed to move along straight lines (beams)

$$L_{\phi,s} := \{s\vartheta_{\phi} + t\vartheta_{\phi}^{\perp} \in \mathbb{R}^2 \mid t \in \mathbb{R}\} \quad (1)$$

for $(\phi, s) \in \mathcal{S} := [0, \pi[\times]-1, 1[$ (called the sinogram domain, having an angular and a detector component), where $\vartheta_\phi := (\cos(\phi), \sin(\phi)) \in \mathbb{R}^2$ is the unit vector associated with the angle ϕ and $\vartheta_\phi^\perp := (-\sin(\phi), \cos(\phi)) \in \mathbb{R}^2$ is the direction rotated by 90 degrees counterclockwise; see Figure 1. The beam's loss of intensity is the accumulation of losses caused by the beam's interaction with the patient's mass within the body. This accumulation is commonly modeled by the Radon transform [6,15] (in this context also called the forward projection), $\mathcal{R}: L^2(\Omega) \rightarrow L^2(\mathcal{S})$ according to

$$[\mathcal{R}f](\phi, s) := \int_{\Omega} f(x) d\mathcal{H}^1 \llcorner L_{\phi,s}(x) = \int_{-\sqrt{1-s^2}}^{\sqrt{1-s^2}} f(s\vartheta_\phi + t\vartheta_\phi^\perp) dt \quad (2)$$

for $f \in L^2(\Omega)$ and $(\phi, s) \in \mathcal{S}$ (where $\mathcal{H}^1 \llcorner L_{\phi,s}$ denotes the one-dimensional Hausdorff measure restricted to $L_{\phi,s}$), i.e., \mathcal{R} is a collection of line integrals. Thus, the tomographic reconstruction corresponds to the solution of the inverse problem $\mathcal{R}f = g$ for known measurements g and unknown mass density distributions f .

While there is a direct inversion called the filtered backprojection [15], many more evolved reconstruction techniques are iterative, e.g., iterative algebraic reconstruction algorithms [3,9,18] and solution algorithms for convex optimization problems (e.g., total variation regularized reconstructions) [7,12,19]. These iterative methods also involve the adjoint operator $\mathcal{R}^*: L^2(\mathcal{S}) \rightarrow L^2(\Omega)$ (called the backprojection [15]), which, given $g \in L^2(\mathcal{S})$, reads

$$[\mathcal{R}^*g](x) := \int_0^\pi g(x \cdot \vartheta_\phi, \phi) d\phi \quad \text{for } x \in \Omega. \quad (3)$$

Only finite amounts of data can be measured and processed in practical applications. Thus, proper discretization \mathcal{R}_δ for \mathcal{R} (and the adjoints) is imperative, where δ describes the degree of discretization. For us, $\delta = (\delta_x, \delta_\phi, \delta_s)$ denotes the spatial resolution of reconstructions, and the angular and detector resolutions of measured data (we think of both reconstructions and measurements as images). The expectation is that with ever finer resolution ($\delta \rightarrow 0$), also the approximation gets arbitrarily good (i.e., $\mathcal{R}_\delta \rightarrow \mathcal{R}$ in some sense). The most widespread discretization framework uses the ray-driven Radon transform $\mathcal{R}_\delta^{\text{rd}}$ [8,20,21] and the pixel-driven backprojection $\mathcal{R}_\delta^{\text{pd}^*}$ [4,16,17,23] (we call it an rd-pd* approach) with balanced resolutions, i.e., $\delta_x \approx \delta_s$. Note that usually δ_ϕ and δ_s are determined from the measurements, while δ_x is somewhat selectable. The ray-driven approach discretizes line integrals by splitting them into sections associated with the intersections of the line with pixels, while the pixel-driven backprojection is based on a linear interpolation approximation of (3) (see Figure 3). There is also a ray-driven backprojection and a pixel-driven ray-driven Radon transform as the adjoint operators of the aforementioned operators. However, they do not see much use due to being supposed poor approximations that create artifacts [13]. Not using the forward and backprojections from the same framework (e.g., rd-rd* or pd-pd*) can potentially harm iterative solvers [14,22].

However, this danger seems to be outweighed in practice by the supposed better approximation performance of rd-pd* methods. There is little rigorous

analysis of approximation errors, and anecdotal knowledge of performance is much more prevalent. [4] rigorously discussed approximation errors for pixel-driven methods in the case that the spatial resolution δ_x is asymptotically smaller than the detector resolution δ_s , finding convergence in the operator norm. Thus, a pd-pd* approach is justified when $\frac{\delta_x}{\delta_s} \rightarrow 0$ (both avoiding the unmatched operator issue, while yielding proper approximations). However, in practice, it is much more common to use balanced resolutions (i.e., $\delta_x \approx \delta_s$). This paper will partially justify the use of rd-pd* approaches for balanced resolutions by describing a novel interpretation of ray-driven methods that allows for much more structured analysis. In particular, based on these novel interpretations, we announce convergence results in the strong operator topology in Theorem 1 (thus substantiating heuristic notions of approximation performance). The rigorous proof of the statement is available at arXiv [1], with a corresponding journal article in preparation. Some of these results were already presented in the doctoral thesis [11].

2 Discretization Approaches for the Radon transform

We start by discretizing the spatial domain $\Omega = B(0, 1)$ and the sinogram domain $\mathcal{S} = [0, \pi[\times]-1, 1[$ into ‘pixels’; one can think of data and reconstructions as digital two-dimensional images; see Figure 1. We fix $N_x \in \mathbb{N}$ and set $\delta_x = \frac{2}{N_x}$. We define the spatial pixel centers $x_{ij} := (\frac{2i+1}{N_x} - 1, \frac{2j+1}{N_x} - 1) = ((i + \frac{1}{2})\delta_x - 1, (j + \frac{1}{2})\delta_x - 1)$ for $i, j \in [N_x] := \{0, \dots, N_x - 1\}$ and $X_{ij} := x_{ij} + [-\frac{\delta_x}{2}, \frac{\delta_x}{2}]^2$ denotes the corresponding squared spatial pixel with side-length δ_x . We consider a finite number $N_\phi \in \mathbb{N}$ of angles $\phi_0 < \dots < \phi_{N_\phi-1} \in [0, \pi[$ and associate them with the angular pixel $\Phi_q := [\frac{\phi_{q-1} + \phi_q}{2}, \frac{\phi_q + \phi_{q+1}}{2}[$ for $q \in [N_\phi]$, where we understand $\phi_{-1} = \phi_{N_\phi-1} - \pi$ and $\phi_{N_\phi} = \phi_0 + \pi$. (Note that potentially $\Phi_0 \not\subset [0, \pi[$ or $\Phi_{N_\phi-1} \not\subset [0, \pi[$, in which case we tacitly π periodically project them onto $[0, \pi[$.) Correspondingly, we set $\delta_\phi := \max_{q \in [N_\phi]} |\Phi_q|$. For the sake of readability, we write ϑ_q when we mean ϑ_{ϕ_q} for the unit vector associated with ϕ_q . We assume a fixed number $N_s \in \mathbb{N}$ of detector pixels and set $\delta_s = \frac{2}{N_s}$. The associated (equispaced) detector pixels are $S_p := s_p + [-\frac{\delta_s}{2}, \frac{\delta_s}{2}[$ for $p \in [N_s]$ with centers $s_p := \frac{2p+1}{N_s} - 1 = (p + \frac{1}{2})\delta_s - 1$. Hence, we have discretized the domain Ω into a Cartesian $N_x \times N_x$ grid with resolution δ_x , while the sinogram space \mathcal{S} contains $N_\phi \times N_s$ rectangular pixels $\Phi_q \times S_p$ for $q \in [N_\phi]$ and $p \in [N_s]$, i.e., with angular resolution δ_ϕ and detector resolution δ_s , see Figure 1. We notationally combine all these resolutions to $\delta = (\delta_x, \delta_\phi, \delta_s) \in \mathbb{R}^+ \times \mathbb{R}^+ \times \mathbb{R}^+$, and N_x, N_ϕ and N_s are tacitly chosen accordingly.

One can naturally associate pixels values of an image representing $f \in L^2(\Omega)$ with average values $f_{ij} := \frac{1}{\delta_x^2} \int_{X_{ij}} f(x) dx$. Moreover, one can consider the associated (pixelized) functions $f_\delta = \sum_{i,j=0}^{N_x-1} f_{ij} u_{ij}$ in $U_\delta := \text{span}\{u_{ij}\} \cong \mathbb{R}^{N_x^2}$ with $u_{ij} := \chi_{X_{ij}} - \frac{1}{2} \chi_{\partial X_{ij}}$, where $\chi_M(x)$ equals 1 if $x \in M$ and zero otherwise, and ∂X_{ij} denotes the boundary of X_{ij} . Analogously we define $V_\delta :=$

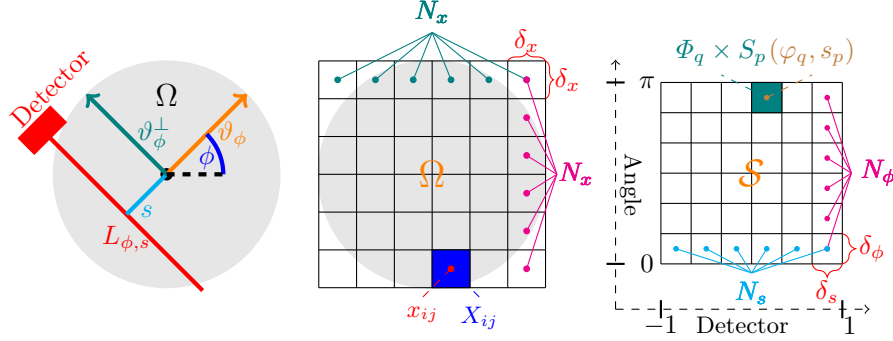


Fig. 1. On the left is the geometry of the Radon transform; in the middle is the discretization of the spatial domain Ω into pixels X_{ij} with width $\delta_x \times \delta_x$; on the right is the discretization of the sinogram domain \mathcal{S} into pixels $\Phi_q \times S_p$ of width $|\Phi_q| \times \delta_s$.

$\text{span}\{\chi_{\Phi_q \times S_p}\}$ for discrete sinograms. Discretizations of \mathcal{R} translate to a matrix $A \in \mathbb{R}^{(N_\phi \cdot N_s) \times N_x^2}$, where A_{qpij} denotes the weight attributed to a pixel X_{ij} in the calculation of L_{ϕ_q, s_p} (q and p determine a row in A , while i and j determine a column). Interpreting A as a mapping from $U_\delta \subset L^2(\Omega)$ to $V_\delta \subset L^2(\mathcal{S})$, we can understand the discretizations as finite rank operators between L^2 spaces, thus allowing for a proper comparison with \mathcal{R} .

In order to compute $[\mathcal{R}f](\phi, s)$, one has to take relatively few values (the values of f along $L_{\phi, s}$) into account; therefore also the A_{qpij} should be non-zero only for pixels X_{ij} that are close to L_{ϕ_q, s_p} . To this end, we will set the weights A_{qpij} using the following weight functions.

Definition 1. Given δ and $\phi \in [0, \pi[$, we set $\bar{s}(\phi) := \frac{\delta_x}{2} (|\cos(\phi)| + |\sin(\phi)|)$, $\underline{s}(\phi) := \frac{\delta_x}{2} (|\cos(\phi)| - |\sin(\phi)|)$ and $\kappa(\phi) := \min \left\{ \frac{1}{|\cos(\phi)|}, \frac{1}{|\sin(\phi)|} \right\}$ (with $\frac{1}{0} = \infty$). We define the ray-driven weight function for $t \in \mathbb{R}$ according to

$$\omega_\delta^{\text{rd}}(\phi, t) := \frac{1}{\delta_x} \begin{cases} \frac{\bar{s}(\phi) - |t|}{\delta_x |\cos(\phi) \sin(\phi)|} & \text{if } |t| \in [\underline{s}(\phi), \bar{s}(\phi)[, \\ \kappa(\phi) & \text{if } |t| \in \llbracket \underline{s}(\phi), \\ \frac{1}{2} & \text{if } \phi \in \{0, \frac{\pi}{2}\} \text{ and } |t| = \bar{s}(\phi), \\ 0 & \text{else.} \end{cases} \quad (4)$$

Moreover, we define the pixel-driven weight function to be

$$\omega_\delta^{\text{pd}}(\phi, t) = \omega_\delta^{\text{pd}}(t) := \frac{1}{\delta_s^2} \max\{\delta_s - |t|, 0\} \quad \text{for } \phi \in [0, \pi[, t \in \mathbb{R}. \quad (5)$$

For the ray-driven method, one typically uses weights $A_{qpij} := \mathcal{H}^1(X_{ij} \cap L_{\phi_q, s_p})$ (i.e., the intersection length of line and pixel) computed in an iterative manner following the ray [8]. The novel function $\delta_x^2 \omega_\delta^{\text{rd}}(\phi_q, x_{ij} \cdot \vartheta_q - s_p)$ is a closed form of this weight, allowing more structured analysis.

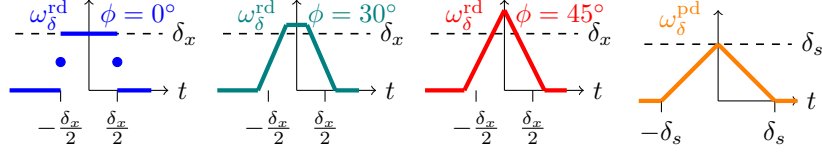


Fig. 2. Depiction of the ray-driven weight function $t \mapsto \delta_x^2 \omega_\delta^{\text{rd}}(\phi, t)$ for fixed $\phi \in \{0^\circ, 30^\circ, 45^\circ\}$. On the right, the depiction of the pixel-driven weight $t \mapsto \delta_s^2 \omega_\delta^{\text{pd}}(t)$.

Definition 2. Given a (weight) function $\omega: \mathcal{S} \rightarrow \mathbb{R}$, we define the convolutional Radon transform $\mathcal{R}_\omega: L^2(\Omega) \rightarrow L^2(\mathcal{S})$, such that, for a function $f \in L^2(\Omega)$,

$$[\mathcal{R}_\omega f](\phi, s) := \sum_{q=0}^{N_\phi-1} \sum_{p=0}^{N_s-1} \chi_{\Phi_q \times S_p}(\phi, s) \sum_{i,j=0}^{N_x-1} \omega(\phi_q, x_{ij} \cdot \vartheta_q - s_p) \int_{X_{ij}} f(x) dx. \quad (6)$$

The ray-driven Radon transform $\mathcal{R}_\delta^{\text{rd}}$ and pixel-driven Radon transform $\mathcal{R}_\delta^{\text{pd}}$ are defined as special cases of \mathcal{R}_ω with $\omega = \omega_\delta^{\text{rd}}$ or $\omega = \omega_\delta^{\text{pd}}$, respectively. The corresponding ray-driven or pixel-driven backprojections $\mathcal{R}_\delta^{\text{rd}*}$ and $\mathcal{R}_\delta^{\text{pd}*}$ are special cases of the convolutional backprojection $\mathcal{R}_\omega^*: L^2(\mathcal{S}) \rightarrow L^2(\Omega)$ according to

$$[\mathcal{R}_\omega^* g](x) = \sum_{i,j=0}^{N_x-1} \chi_{X_{ij}}(x) \sum_{q=0}^{N_\phi-1} \sum_{p=0}^{N_s-1} \omega(\phi_q, x_{ij} \cdot \vartheta_q - s_p) \int_{\Phi_q \times S_p} g(\phi, s) d(\phi, s) \quad (7)$$

for $g \in L^2(\mathcal{S})$ when setting ω to $\omega_\delta^{\text{rd}}$ or $\omega_\delta^{\text{pd}}$, respectively.

Note that these definitions are operators between L^2 spaces, whose corresponding matrices A coincide with the classical interpretation of these methods in the literature as intersection lengths as weights and linear interpolation, respectively; see Figure 3. Also, (6) and (7) show that from a certain point of view, the ray-driven and pixel-driven methods are actually quite similar. Therefore, they can also be implemented using structurally analogous algorithms with similar degrees of parallelization.

3 Theoretical Results

Lemma 1. Given δ , and $f_\delta \in U_\delta$, for all $\hat{q} \in [N_\phi]$ and $\hat{p} \in [N_s]$, we have

$$[\mathcal{R} f_\delta](\phi_{\hat{q}}, s_{\hat{p}}) = [\mathcal{R}_\delta^{\text{rd}} f_\delta](\phi_{\hat{q}}, s_{\hat{p}}). \quad (\text{exact}^{\text{rd}})$$

Moreover, for fixed $\hat{i}, \hat{j} \in [N_x]$ such that $x_{\hat{i}\hat{j}} \cdot \vartheta_{\hat{q}} \in [s_0, s_{N_s-1}]$, we have

$$\sum_{p=0}^{N_s-1} \omega_\delta^{\text{pd}}(x_{\hat{i}\hat{j}} \cdot \vartheta_{\hat{q}} - s_p) = \frac{1}{\delta_s} \quad (\text{intpol}^{\text{pd}})$$

with exactly two non-zero summands \hat{p} and $\hat{p} + 1$ if $x_{\hat{i}\hat{j}} \cdot \vartheta_{\hat{q}} \in]s_{\hat{p}}, s_{\hat{p}+1}[$ and a single non-zero summand \hat{p} if $x_{\hat{i}\hat{j}} \cdot \vartheta_{\hat{q}} = s_{\hat{p}}$.

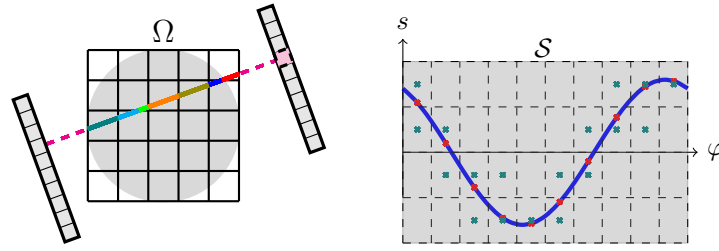


Fig. 3. Illustration of the ray-driven Radon transform (left) and pixel-driven backprojection (right). In the former, integration along a straight line is split into the sum of integrals along the intersections with pixels. The pixel-driven backprojection discretizes the angular integral (3) (along the blue curve $(x \cdot \vartheta_\phi, \phi)$) by a finite sum of angular evaluations $(x \cdot \vartheta_q, \phi_q)$ (red dots), with linear interpolation in the detector dimension (using the points represented by the green dots).

One can interpret (exactrd) as the ray-driven forward being precise for piecewise constant functions (images) in the detector pixel centers. The ray-driven and pixel-driven discretizations have been known for decades, but no rigorous convergence results were presented. Theorem 1 complements anecdotal reports on the performance of these discretization approaches, announcing convergence in the strong operator topology (the proof is found at [1]).

Theorem 1. *Let $(\delta^n)_{n \in \mathbb{N}} = (\delta_x^n, \delta_\phi^n, \delta_s^n)_{n \in \mathbb{N}}$ be a sequence of discretization parameters with $\delta^n \xrightarrow{n \rightarrow \infty} 0$ (componentwise) and let $c > 0$ be a constant. If $\frac{\delta_s^n}{\delta_x^n} < c$ for all $n \in \mathbb{N}$, then, for any $f \in L^2(\Omega)$, we have*

$$\lim_{n \rightarrow \infty} \|\mathcal{R}f - \mathcal{R}_{\delta^n}^{\text{rd}} f\|_{L^2} = 0. \quad (\text{conv}^{\text{rd}})$$

If the sequence $(\delta^n)_{n \in \mathbb{N}}$ satisfies $\frac{\delta_s^n}{\delta_x^n} \xrightarrow{n \rightarrow \infty} 0$, then, for each $g \in L^2(\mathcal{S})$, we have

$$\lim_{n \rightarrow \infty} \|\mathcal{R}^* g - \mathcal{R}_{\delta^n}^{\text{rd}*} g\|_{L^2} = 0. \quad (\text{conv}^{\text{rd}*})$$

If $\frac{\delta_x^n}{\delta_s^n} \leq c$ for all $n \in \mathbb{N}$, then, for each $g \in L^2(\mathcal{S})$, we have

$$\lim_{n \rightarrow \infty} \|\mathcal{R}^* g - \mathcal{R}_{\delta^n}^{\text{pd}*} g\|_{L^2} = 0. \quad (\text{conv}^{\text{pd}*})$$

Remark 1. Note that both (convrd) and (conv^{pd*}) are applicable in the case $\delta_x^n \approx \delta_s^n$ (or equivalently $N_x \approx N_s$), so using the rd-pd* approach in the balanced resolution case is justified in the sense that we have pointwise convergence of the operators. Note that the convergence described in Theorem 1 is not necessarily uniform, i.e., the convergence speed could depend on the specific f and g .

4 Insights into Weight Functions via Simulations

Throughout this section, we use small numerical experiments to highlight certain properties of the weight functions and show how they impact the discretized

operators. All calculations were implemented in Python using PyOpenCL with the pixel-driven methods from Gratopy [5], and with a custom ray-driven implementation in an analogous style. All calculations were executed on a 12th Gen Intel(R) Core(TM) i7-12650H in parallel with single precision. The code is available as a GitHub repository at [2]. We consider angles $\phi_q = \pi \frac{q}{N_\phi}$ for $q \in [N_\phi]$. In our illustrations below, we always assume (and only visualize) $x, x_{ij} \in B(0, 0.9)$ to avoid technical issues occurring at the boundary $\partial\Omega$ that are not central to our observations.

Example 1

Let us start with the most trivial example for backprojections; we consider the constant sinogram $g(\phi, s) = 1$ for $(\phi, s) \in \mathcal{S}$. It is trivial to see that the backprojection satisfies $[\mathcal{R}^* g](x) = \pi$ (as the integrand in (3) is constant). When looking at (7) for this concrete example, we would like to have

$$\sum_{q=0}^{N_\phi-1} \sum_{p=0}^{N_s-1} \delta_s |\phi_q| \omega(\phi_q, x_{ij} \cdot \vartheta_q - s_p) \stackrel{\text{per}}{\stackrel{\text{def}}{=} [\mathcal{R}_\omega^* g](x_{ij}) = [\mathcal{R}^* g](x_{ij}) = \pi. \quad (8)$$

(Requesting (8) to hold for all $x \in \Omega$ seems quite naturally then.) When (8) is satisfied, the method will be precise for this concrete example. And the pixel-driven backprojection (i.e., with $\omega = \omega_\delta^{\text{pd}}$) satisfies (8) due to (intpol^{pd}) (for $\|x\| \leq |s_0|$) and since $\sum_{q=0}^{N_\phi-1} |\Phi_q| = \pi$. Hence, the pixel-driven backprojection should be correct up to machine precision ($\approx 10^{-6}$) for this concrete example, which numerical experiments confirm.

In contrast, for the ray-driven methods, it is unclear whether (8) holds. Figures 4 a), b) and c) depict the error of simulations using the ray-driven backprojections, revealing some geometric patterns whose amplitude does not decrease with increased N_x and N_s under balanced resolutions (i.e., $N_x = N_s$). Also, the corresponding L^2 error stays virtually the same. The relative error is roughly one percent, i.e., not huge. Still, this illustrates a potential issue that appears to not be solved by increasing resolutions. Note that the structured nature of the error suggests this is not caused by random rounding errors, but has a deeper cause in the weight function $\omega_\delta^{\text{rd}}$.

Looking at Figures 4 c), d) and e), we note that the error appears to reduce with increasing number of angles, though not very quickly. As illustrated in the pixel-driven backprojections' precision, the angular resolution should not be a natural limiting factor for this example. In spite of that, for the ray-driven method it appears so. This can be understood as follows, (8) is a mean value of $\phi \mapsto \sum_{p=0}^{N_s-1} \delta_s \omega(\phi, x_{ij} \cdot \vartheta_\phi - s_p)$, and while this does not have a fixed value for all angles ϕ or points x_{ij} , it still averages out to 1. Thus, the more angles, are considered the closer is (8) to be satisfied.

According to (conv^{rd*}), if $\delta_x \ll \delta_s$ the method should converge. And indeed, as depicted in Figure 4 f), the error reduces significantly (by a factor of 10) when considering $N_x = 1000$ and $N_s = 4000$. It might seem counter-intuitive

that using coarser spatial resolution (compared to 4 c)) yields a significantly better approximation, but this is in line with ($\text{conv}^{\text{rd}*}$).

Approximation Errors of Ray-Driven Backprojections for Example 1

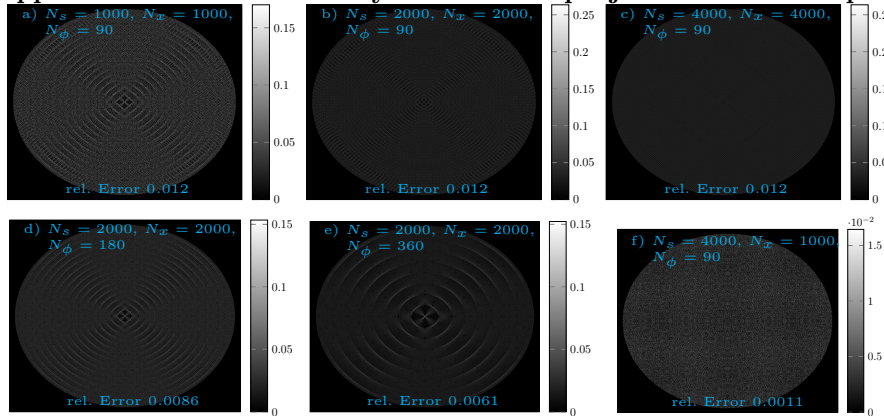


Fig. 4. Illustration of the error incurred by ray-driven backprojections for Example 1. In the first row, a balanced resolutions setting with fixed $N_\phi = 90$ but increasing $N_x = N_s$ is shown. The amplitude of the errors and the relative L^2 error, do not reduce with finer spatial and detector resolutions. In d) and e), we increase N_ϕ to $N_\phi = 180$ and $N_\phi = 360$, yielding slight improvements. Lastly, we depict the error when reducing the spatial resolution to $N_x = 1000$ while keeping $N_s = 4000$ detector pixels, leaving the balanced resolution setting and significantly reducing the error.

Example 2

We fix some $\hat{q} \in [N_\phi]$ and consider $g_{\hat{q}}(\phi, s) = \frac{1}{|\Phi_{\hat{q}}|}$ for $s \in]-1, 1[$ and $\phi \in \Phi_{\hat{q}}$ and zero otherwise, i.e., the sinogram has only very small angular support. Straight-forward calculation shows $[\mathcal{R}^* g_{\hat{q}}](x) = 1$ for all $x \in \Omega$.

Hence, in order for the convolutional approximations of this example (with the specific \hat{q}) to be precise, one would require

$$\sum_{p=0}^{N_s-1} \delta_s \omega(x_{ij} \cdot \vartheta_{\hat{q}} - s_p, \phi_{\hat{q}}) = 1. \quad (9)$$

(Naturally, \hat{q} was arbitrary, so we would want (9) to hold for all angles.) For the pixel-driven method, (9) holds via ($\text{intpol}^{\text{pd}}$), and therefore, the pixel-driven method is again precise (up to machine precision).

The averaging with respect to the angles described in Example 1 that moderated (8) does not apply here. Therefore, the issue seen in Example 1 becomes

much more severe for the ray-driven method. In fact, a key step in proving convergence of the ray-driven backprojection in ($\text{conv}^{\text{rd}*}$) is to show that ray-driven weight functions asymptotically satisfy (9) when $\delta_s \ll \delta_x$.

Figures 5 a) and b) depict the errors of the ray-driven backprojection (with \hat{q} such that $\phi_{\hat{q}} = \frac{\pi}{4}$), showing again certain patterns which are much more prominent than they were in Example 1. They cause a relative L^2 error of 19% and again appear to remain while in the balanced resolutions setting with finer resolutions. However, increasing the number of angles does not improve things this time. Again, choosing N_x significantly smaller than N_s reduces this error significantly (by a factor of roughly 30); see Figure 5 c).

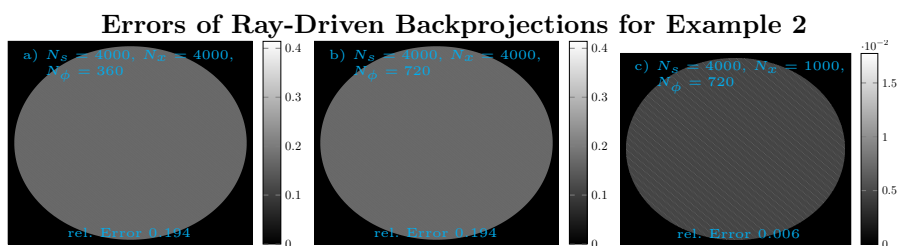


Fig. 5. Illustration of errors for Example 2, depicting the approximation errors of ray-driven backprojection with \hat{q} such that $\phi_{\hat{q}} = \frac{\pi}{4}$. Under balanced resolutions in a) and b), these errors are very significant and do not reduce with an increased number of angles. In c), we leave the balanced resolution setting, reducing errors significantly.

It might be possible to translate these considerations into a rigorous construction of a function g (only being non-zero on tacitly chosen angles) with $\|\mathcal{R}^*g - \mathcal{R}_\delta^{\text{rd}*}g\| \geq c\|g\|$ for some constant $c > 0$ and all N_x, N_s such that $N_x \approx N_s$ and $\delta_\phi \rightarrow 0$. If that was the case, the ray-driven Radon transform could not converge to the Radon transform in the operator norm. Then, for any δ there would be a function $f = f(\delta)$ such that $\|\mathcal{R}f - \mathcal{R}_\delta^{\text{rd}}f\| \geq c\|f\|$, i.e., no uniform convergence would hold and no matter how fine the resolution, there would always be functions for which the ray-driven Radon transform is a poor approximation.

Example 3

Next, we consider the sinogram $g(\phi, s) = s$ for all $\phi \in [0, \pi[$ and $s \in \mathbb{R}$ with

$$[\mathcal{R}^*g](x) = \int_0^\pi \mathbf{x} \cos(\phi) + \mathbf{y} \sin(\phi) d\phi = 2\mathbf{y}, \quad (10)$$

where $x = (\mathbf{x}, \mathbf{y})$. Since the pixel-driven method is a linear interpolation (see ($\text{intpol}^{\text{pd}}$)), and g is linear in the detector dimension and constant in the angular dimension, one might suspect that $\mathcal{R}_\delta^{\text{pd}*}$ is again accurate up to machine

precision. However, this would be a fallacy. One can explicitly calculate the pixel-driven backprojection to be

$$[\mathcal{R}_\delta^{\text{pd}^*} g](x_{ij}) = \sum_{q=0}^{N_\phi-1} \mathbf{x}_i \cos(\phi_q) + \mathbf{y}_j \sin(\phi_q), \quad (11)$$

where $x_{ij} = (\mathbf{x}_i, \mathbf{y}_j)$. Hence, the error that the pixel-driven backprojection suffers is the error of the Riemann sum of the integrals in (10), i.e.,

$$[\mathcal{R}^* g](x_{ij}) - [\mathcal{R}_\delta^{\text{pd}} g](x_{ij}) = -\mathbf{x}_i \sum_{q=0}^{N_\phi-1} \cos(\phi_q) + \mathbf{y}_j \left(2 - \sum_{q=0}^{N_\phi-1} \sin(\phi_q) \right). \quad (12)$$

Thus, the pixel-driven backprojection can lead to highly structured errors related to how well these Riemann sums approximate the cosine and sine integrals. In particular, although g does not depend on ϕ , the angular resolution can have an impact here.

For our numerical experiments, we started with the naive choice $\phi_0 = 0^\circ$, $\phi_1 = 1^\circ, \dots, \phi_{179} = 179^\circ$. Then, the error of the Riemann sum approximating the cosine integral is roughly $\pi/180 \approx 0.0174$ while the Riemann sum of the sine terms equals roughly 1.99995. Hence, when computing the pixel-driven method for this example, the error is dominated by the linear $0.0174 \mathbf{x}_i$, see Figure 6 a).

If we shift the considered angles by 0.5° , i.e., $\phi_0 = 0.5^\circ$, $\phi_1 = 1.5^\circ$, and so on, by symmetry the cosine Riemann sum is zero, while the sine Riemann sum's error is roughly $2 \cdot 10^{-5}$. Hence, the error is dominated by $2\mathbf{y}_j 10^{-5}$, which overall reduces the approximation error substantially (roughly by a factor of 10^{-3}). This structure is also observed in our simulations in Figure 6 b). Note that neither of the presented backprojections is terrible, however, their difference and the structure of the errors is unexpected.

Naturally, for real data, such considerations cannot be taken into account (as we have no insight into the functions we are integrating). Nonetheless, this gives some interesting insight that even though sinograms are not changing with respect to the angular domain, the angular discretization can significantly impact approximation errors. Theorem 1 suggests that with increasing number of angles this issue reduces (irrespective of the specific angles). In contrast, in the ray-driven backprojection the error is not as structured (see Figure 6 c)), suggesting that factors other than the Riemann sum drive the error.

5 Conclusion and Outlook

This paper presented a novel interpretation of ray-driven and pixel-driven methods as ‘convolutional discretizations’, suggesting in some sense the methods are more alike than previously thought. Moreover, we announced novel convergence statements in the strong operator topology in Theorem 1. These results give a theoretical foundation for the widespread use of ray-driven forward and pixel-driven backprojection operators under balanced resolutions (previously based

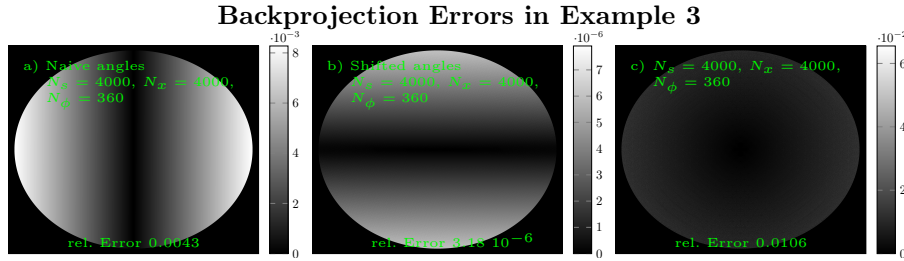


Fig. 6. Illustration of the error of backprojections for Example 3. In a) the pixel-driven backprojections’ errors with the naive angles, and in b) with the described angle shift. The ray-driven backprojection’s error is depicted in c). As can be seen the pixel-driven methods error significantly depends on the angles.

on anecdotal approximation properties). These anecdotes also suggest that ray-driven backprojections and pixel-driven forward projections do not converge. While certainly no proof, our simulations support the former. Hence, the presented results might suggest that the combination of ray-driven and pixel-driven methods is the best one can do while maintaining the balanced resolution setting.

The convergence results are probably extendable to other types of tomography (with fanbeam or conebeam operators), and might be the topic of future investigations. Note that this work did not address the issue of unmatched operators. However, unmatched operators may be preferable if the alternative uses non-approximating discretizations.

The convergence result ($\text{conv}^{\text{rd}*}$) shows that while the ray-driven backprojection might be unsuitable for balanced resolutions, it approximates the backprojection if $\frac{\delta_s}{\delta_x} \rightarrow 0$. Thus, future works might investigate if convergence in the operator norm is achieved in that setting. Moreover, Example 2 might yield a way to show that ray-driven methods do not converge in the operator norm when using balanced resolutions, and thus might also merit future investigations.

Acknowledgments. RH was partially supported by The Villum Foundation (Grant No.25893) and partially by the International Research Training Group “Optimization and Numerical Analysis for Partial Differential Equations with Nonsmooth Structures,” funded by the German Research Council (DFG) and Austrian Science Fund (FWF) grant W1244.

References

1. *: This is a placeholder for the archive not yet uploaded containing the rigorous proof of theorem 1. ArXiv (2025)
2. *: This is a placeholder for the github repository not yet uploaded containing the code with which the simulations where performed. GITHUB (2025)
3. Andersen, A.H., Kak, A.C.: Simultaneous Algebraic Reconstruction Technique (SART): A superior implementation of the ART algorithm. Ultrasonic Imaging **6**(1), 81–94 (1984)

4. Bredies, K., Huber, R.: Convergence analysis of pixel-driven radon and fanbeam transforms. *SIAM Journal on Numerical Analysis* **59**(3), 1399–1432 (2021). <https://doi.org/10.1137/20M1326635>
5. Bredies, K., Huber, R.: Gratomy 0.1 release candidate 1 [software] (2021). <https://doi.org/10.5281/zenodo.5221443>
6. Deans, S.R.: *The Radon Transform and Some of Its Applications*. Krieger Publishing Company (1993)
7. Dong, B., Li, J., Shen, Z.: X-ray CT image reconstruction via wavelet frame based regularization and Radon domain inpainting. *Journal of Scientific Computing* **54**(2), 333–349 (2013). <https://doi.org/10.1007/s10915-012-9579-6>
8. Gao, H.: Fast parallel algorithms for the x-ray transform and its adjoint. *Medical Physics* **39**(11), 7110–7120 (2012). <https://doi.org/10.1118/1.4761867>
9. Gilbert, P.: Iterative methods for the three-dimensional reconstruction of an object from projections. *Journal of Theoretical Biology* **36**(1), 105–117 (1972)
10. Hsieh, J.: *Computed Tomography: Principles, Design, Artifacts, and Recent Advances*. WA: SPIE — The International Society for Optical Engineering (2009)
11. Huber, R.: Pixel-driven projection methods’ approximation properties and applications in electron tomography. PhD thesis, University of Graz, Austria (2022)
12. Huber, R., Haberfehlner, G., Holler, M., Kothleitner, G., Bredies, K.: Total generalized variation regularization for multi-modal electron tomography. *Nanoscale* **11**, 5617–5632 (2019). <https://doi.org/10.1039/C8NR09058K>
13. Liu, R., Fu, L., De Man, B., Yu, H.: Gpu-based branchless distance-driven projection and backprojection. *IEEE Transactions on Computational Imaging* **3**(4), 617–632 (2017). <https://doi.org/10.1109/TCI.2017.2675705>
14. Lorenz, D., Schneppe, F.: Chambolle–pock’s primal-dual method with mismatched adjoint. *Applied Mathematics & Optimization* **87**(2) (2023). <https://doi.org/10.1007/s00245-022-09933-5>
15. Natterer, F.: *The Mathematics of Computerized Tomography*. Society for Industrial and Applied Mathematics, Philadelphia (2001)
16. Peters, T.M.: Algorithms for fast back- and re-projection in computed tomography. *IEEE Transactions on Nuclear Science* **28**(4), 3641–3647 (1981). <https://doi.org/10.1109/TNS.1981.4331812>
17. Qiao, Z., Redler, G., Gui, Z., Qian, Y., Epel, B., Halpern, H.: Three novel accurate pixel-driven projection methods for 2D CT and 3D EPR imaging. *Journal of X-ray science and technology* **26**(1), 83–102 (2017)
18. Scales, J.: Tomographic inversion via the conjugate gradient method. *Geophysics* **52**, 179–185 (1987). <https://doi.org/10.1190/1.1442293>
19. Scherzer, O., Grasmair, M., Grossauer, H., Haltmeier, M., Lenzen, F.: *Variational Methods in Imaging*. Springer, 1 edn. (2008)
20. Siddon, R.L.: Fast calculation of the exact radiological path for a three-dimensional CT array. *Medical Physics* **12**(2), 252–255 (1985)
21. Sundermann, E., Jacobs, F., Christiaens, M., De Sutter, B., Lemahieu, I.: A fast algorithm to calculate the exact radiological path through a pixel or voxel space. *Journal of Computing and Information Technology* **6**, 89–94 (1998)
22. Zeng, G.L., Gullberg, G.T.: Unmatched projector/backprojector pairs in an iterative reconstruction algorithm. *IEEE Trans. Med. Imaging* **19**(5), 548–555 (2000). <https://doi.org/10.1109/42.870265>
23. Zhuang, W., Gopal, S.S., Hebert, T.J.: Numerical evaluation of methods for computing tomographic projections. *IEEE Transactions on Nuclear Science* **41**(4), 1660–1665 (1994). <https://doi.org/10.1109/23.322963>